

Influence of the polarization in grazing scattering of fast helium atoms from LiF(001) surfaces.

M.S. Gravielle¹ and J.E. Miraglia¹

¹*Instituto de Astronomía y Física del Espacio, CONICET,
Casilla de Correo 67, Sucursal 28, 1428 Buenos Aires, Argentina, and
Dpto. de Física, FCEN, Universidad de Buenos Aires, Buenos Aires, Argentina.
(Dated: January 22, 2020)*

Grazing scattering of neutral atoms from insulator surfaces is investigated in the intermediate velocity range, in which interference effects have been recently observed. To describe this process we introduce a distorted-wave method, based on the use of the eikonal wave function, which takes into account the phase of the scattering state along the classical projectile path. The eikonal theory is applied to evaluate the angular distribution of few keV helium atoms after impinging on a LiF(001) surface along low-index crystallographic directions. The interest focuses on the role played by the projectile polarization produced by cations and anions of the crystal surface. For the considered collision system we found a polarization channel, corresponding to the direction $\langle 110 \rangle$, which is affected by this effect, while for incidence in the direction $\langle 100 \rangle$ the polarization contribution is nearly negligible. The proposed eikonal approach, including polarization effects, provides angular projectile spectra in reasonable agreement with the experimental data.

PACS numbers:

I. INTRODUCTION

Experimental evidences of interference effects produced during grazing scattering of fast atoms from insulator surfaces were recently presented in Refs. [1, 2, 3]. Under axial surface channeling conditions, reported measurements of scattered projectile distributions display well defined spots, associated with diffraction patterns originated by the periodic structure of the crystal. Even though the diffraction of particles from crystal surfaces has been a well-understood phenomena from the beginning of quantum mechanics, the importance of these experimental results is due to the effect not being expected to be observable for light atoms with energies in the keV range, whose de Broglie wavelengths are some orders of magnitude smaller than the shortest interatomic distance in the crystal.

Two different interference mechanisms have been proposed to explain the experimental observations. The first of them [1, 2] is related to the diffraction by a periodic lattice and relies on the assumption that the projectile motion perpendicular to the axial incidence channel can be decoupled from the parallel one. The semiclassical approach [2] proposed for the description of this mechanism predicts a maximum in the distribution when the component normal to the scattering plane of the final projectile momentum coincides with a reciprocal lattice vector. Such a result, also confirmed by means of a wave packet propagation approach [2], is in accord with the experimental data for the lowest impact energies [1, 2]. The second mechanism [3], called supernumerary rainbow, is originated by the corrugation of the surface potential, which gives rise to a quantum interference between projectiles emerging from the surface with the same direction but reflected at different turning points [4].

To describe the experimentally observed patterns, in

this article we introduce a distorted-wave model, named surface eikonal approximation, which is valid for small de Broglie wavelengths of incident atoms. This method makes use of the eikonal wave function [5] to represent the elastic collision with the surface, while the projectile movement is classically described, taking into account different initial conditions. The surface eikonal approach can be considered as an extension of the well-known Glauber approximation [6] for collisions with corrugated surfaces [7] instead of atoms, but considering axial channeled trajectories. It includes both interference mechanisms and essentially coincides with the semiclassical formalism [4] used in Ref. [3].

The surface eikonal approach is here employed to describe angular distributions of swift He^0 atoms scattered off from a LiF(001) surface, for which there are experimental data available [1, 2, 3]. As the considered process is very sensitive to the description of the surface potential, the aim of the work is to investigate the influence of the polarization on the interference patterns. In our model the interaction of the incident atom with the crystal surface is represented as a sum of individual interatomic potentials, which take into account the contribution of the different ionic centres of the insulator material [8]. To evaluate the interatomic potentials we use the Abrahamson approximation [9], adding the asymptotic contribution of the projectile polarization. The role of the polarization is analyzed for incidence along the $\langle 100 \rangle$ and $\langle 110 \rangle$ channels, finding that polarization effects are important for this latter crystallographic direction. Atomic units ($e^2 = \hbar = m_e = 1$) are used unless otherwise stated.

II. SURFACE EIKONAL APPROXIMATION

Let us consider the grazing impact of an atomic projectile (P), with mass m_P , on a crystal surface (S). As a result of the collision, the projectile with initial momentum \vec{K}_i is elastically scattered from the surface, ending in a final state with momentum \vec{K}_f . The frame of reference is fixed on a target ion belonging to the first atomic layer, with the surface contained in the $x - y$ plane and the \hat{z} versor perpendicular to the surface, aiming towards the vacuum region.

We assume that the state Ψ_i^+ associated with the collision system satisfies the time-independent Schrödinger equation for the Hamiltonian

$$H = -\frac{1}{2m_P} \nabla_{\vec{R}_P}^2 + V_{SP}(\vec{R}_P), \quad (1)$$

where \vec{R}_P denotes the position of the center of mass of the incident atom and V_{SP} is the surface-projectile interaction. As initial condition, when the projectile is far from the surface, Ψ_i^+ tends to the state Φ_i , with $\Phi_j(\vec{R}_P) = (2\pi)^{-3/2} \exp(i\vec{K}_j \cdot \vec{R}_P)$, $j = i(f)$, the initial (final) unperturbed wave function.

The central magnitude to describe the elastic scattering process is the transition matrix, which reads

$$T_{if} = \int d\vec{R}_P \Phi_f^*(\vec{R}_P) V_{SP}(\vec{R}_P) \Psi_i^+(\vec{R}_P). \quad (2)$$

In the energy range of interest, Eq. (2) can be expressed in terms of the classical trajectory of the projectile - $\vec{\mathcal{R}}_P$ - by means of the substitution $\vec{R}_P \cong \vec{\mathcal{R}}_P$, like in the usual semiclassical formalism [10]. The position $\vec{\mathcal{R}}_P$ of the incident atom at a given time t is governed by the Newton equations associated with the potential V_{SP} , verifying the relation $\vec{\mathcal{R}}_P(\vec{R}_{os}, t) = \vec{R}_{os} + Z_o \hat{z} + \int_{-\infty}^t dt' \vec{v}(\vec{R}_{os}, t')$, where $\vec{v}(\vec{R}_{os}, t)$ is the classical velocity of the projectile, $\vec{R}_{os} = (X_o, Y_o, 0)$ identifies its initial position on the surface plane and $Z_o \rightarrow +\infty$. A sketch picture of the projectile path and the coordinate system is displayed in Fig. 1. By replacing the integration variables $\vec{R}_P = (X_P, Y_P, Z_P)$ by the new ones $\{X_o, Y_o, t\}$ in Eq. (2), the transition matrix is expressed as [11]

$$T_{if} = \int d\vec{R}_{os} \int_{-\infty}^{+\infty} dt \left| v_z(\vec{R}_{os}, t) \right| \times \Phi_f^*(\vec{\mathcal{R}}_P) V_{SP}(\vec{\mathcal{R}}_P) \Psi_i^+(\vec{\mathcal{R}}_P), \quad (3)$$

where $v_z(\vec{R}_{os}, t)$ is the component of \vec{v} normal to the surface.

Since the de Broglie wavelength of the incident projectile, $\lambda = 2\pi/K_i$, is sufficiently short compared with the characteristic distance of the surface potential, we

approximate the scattering state Ψ_i^+ by means of the eikonal wave function [5], i.e.

$$\Psi_i^+(\vec{\mathcal{R}}_P) \simeq \chi_i^{(eik)+}(\vec{\mathcal{R}}_P) = \Phi_i(\vec{\mathcal{R}}_P) \exp(-i\eta(\vec{\mathcal{R}}_P)), \quad (4)$$

where $\eta(\vec{\mathcal{R}}_P)$ is the eikonal phase, defined as

$$\eta(\vec{\mathcal{R}}_P(\vec{R}_{os}, t)) = \int_{-\infty}^t dt' V_{SP}(\vec{\mathcal{R}}_P(\vec{R}_{os}, t')). \quad (5)$$

By introducing the function $\chi_i^{(eik)+}$ in Eq. (3) the eikonal transition matrix reads

$$T_{if}^{(eik)} = \frac{1}{(2\pi)^3} \int d\vec{R}_{os} \int_{-\infty}^{+\infty} dt \left| v_z(\vec{R}_{os}, t) \right| \times \exp[-i\vec{Q} \cdot \vec{\mathcal{R}}_P - i\eta(\vec{\mathcal{R}}_P)] V_{SP}(\vec{\mathcal{R}}_P), \quad (6)$$

where $\vec{Q} = \vec{K}_f - \vec{K}_i$ is the projectile momentum transfer and the final momentum \vec{K}_f satisfies the energy conservation, i.e. $K_f = K_i$. The differential probability, per unit of surface area, of elastic scattering with final momentum \vec{K}_f in the direction of the solid angle Ω_f is obtained from Eq. (6) as $dP/d\Omega_f = (2\pi)^4 m_P^2 \left| \tilde{T}_{if}^{(eik)} \right|^2$, where $\tilde{T}_{if}^{(eik)}$ denotes the eikonal T-matrix element, normalized per unit area. Note that the main difference between the usual eikonal scattering amplitude [5, 7] and Eq. (6) arises from the use of axial channeled trajectories instead of straight-line ones.

The first Born T-matrix element can be derived from Eq. (6) by neglecting the eikonal phase; that is, by fixing $\eta(\vec{\mathcal{R}}_P) = 0$. It reads

$$T_{if}^{(Born)} = \frac{1}{(2\pi)^3} \int d\vec{R}_{os} \int_{-\infty}^{+\infty} dt \left| v_z(\vec{R}_{os}, t) \right| \times \exp(-i\vec{Q} \cdot \vec{\mathcal{R}}_P) V_{SP}(\vec{\mathcal{R}}_P). \quad (7)$$

III. INTERACTION POTENTIALS

In this work, the projectile-surface potential is expressed as a sum of individual interatomic potentials, $V(R)$, which represent the interaction of the incident atom with solid ions placed at different lattice sites [8]. Following the Lenz energy functional [12, 13], for the two types of target ions - alkali-metal and halide- the ion-atom interaction is found to be the sum of four terms,

$$V(\vec{R}) = V_{Coul}(\vec{R}) + V_{kin}(\vec{R}) + V_{xch}(\vec{R}) + V_{pol}(\vec{R}). \quad (8)$$

The first term is the well-known electrostatic Coulomb interaction,

$$V_{Coul}(\vec{R}) = \frac{1}{2} \int \int d\vec{r} d\vec{r}' D_T(\vec{r}) \frac{1}{|\vec{r} - \vec{r}'|} D_P(\vec{r}' - \vec{R}), \quad (9)$$

where $D_T(\vec{r}) = Z_T \delta(\vec{r}) - \rho_T(\vec{r})$ and $D_P(\vec{r}) = Z_P \delta(\vec{r}) - \rho_P(\vec{r})$ are the target and projectile charge densities, δ is the Dirac delta function, situated at the position of the nucleus, Z_T (Z_P) is the target (projectile) nucleus charge, and ρ_T (ρ_P) is the target (projectile) electronic density. Note that V_{Coul} is composed by four terms, including the internuclear and electron-electron repulsions as well as the attractive electron-nucleus potentials.

By employing the Abrahamson approximation [9] the second term of Eq.(8), named the kinetic potential, reads

$$V_{kin}(\vec{R}) \frac{1}{2.871} = \int d\vec{r} \left[\rho_T(\vec{r}) + \rho_P(\vec{r} - \vec{R}) \right]^{5/3} \quad (10)$$

$$- \int d\vec{r} \rho_T^{5/3}(\vec{r}) - \int d\vec{r} \rho_P^{5/3}(\vec{r} - \vec{R}).$$

This potential is essentially positive and represents the reaction to the compression of the electronic density, considered as a free-electron gas. The third term describes the exchange potential within the local approximation and it reads

$$V_{sch}(\vec{R}) \frac{(-1)}{0.738} = \int d\vec{r} \left[\rho_T(\vec{r}) + \rho_P(\vec{r} - \vec{R}) \right]^{4/3} \quad (11)$$

$$- \int d\vec{r} \rho_T^{4/3}(\vec{r}) - \int d\vec{r} \rho_P^{4/3}(\vec{r} - \vec{R}).$$

Finally, the fourth term of Eq.(8) takes into account the polarization of the neutral projectile in the presence of the target ion, which is not included in the original Abrahamson model. At large distances the polarization potential is known to behave as $\alpha/2r^4$, while at short distances it is generally reduced with a cut off, which is always of the order of the radius of the atom. We use the following expression for the polarization potential,

$$V_{pol}(\vec{R}) = -\frac{Z_T^{(\infty)} \alpha}{2(R_0^2 + R^2)^2}, \quad (12)$$

with $R_0 = \langle r \rangle_T + \langle r \rangle_P$, where $\langle r \rangle_T$ ($\langle r \rangle_P$) is the target (projectile) mean radius, and $Z_T^{(\infty)}$ is the residual charge of the target ion at long distances, being $Z_T^{(\infty)} = 1$ for Li^+ and $Z_T^{(\infty)} = -1$ for F^- . In Eq.(12), α is the polarizability of the projectile, with $\alpha = 1.38$ a.u. for Helium [14]. Notice that as we are dealing with neutral projectiles, we have not taken into account the dynamic polarization of the surface ion [8] because this effect represents a higher-order correction of the interatomic potential ($\propto r^{-6}$).

IV. RESULTS

We applied the model to neutral helium atoms impinging grazing on a LiF crystal surface under axial surface channeling conditions. The impact energy ranged from 0.2 to 8.6 keV, corresponding to the experiments of Refs. [1, 2, 3]. In the crystal surface, ions belonging to the topmost atomic layer were slightly displaced from their equilibrium positions, in accord with Ref. [15].

To describe the projectile-surface potential we employed the punctual model of Ref. [8], evaluating the He-Li⁺ and He-F⁻ interatomic potentials from Eq.(8). Hartree-Fock Slater wave functions from Clementi-Roetti [16] were used to calculate the electronic densities ρ_T and ρ_P . It allowed us to derive a closed form for V_{Coul} , while V_{kin} and V_{sch} were obtained from numerical integrations. In Fig. 2 it seemed convenient to plot the scaled expression $W(R) = V(R) * R(1 + 2R^3)$ for Li⁺ and F⁻, respectively. From the figure we can differentiate three different regions of the interatomic potentials. As $R \rightarrow 0$, $W(R) \rightarrow Z_T Z_P$ and the sharp increase at the origin corresponds to the electrostatic contribution $V_{Coul}(R)$. The maximum at intermediate distances is mainly due to the statistical contribution, i.e. $V_{kin}(R) + V_{sch}(R)$, while the asymptotic limit as $R \rightarrow \infty$ depends on the polarization, i.e. $W(R) \rightarrow \pm \alpha$, resulting attractive for Li⁺ and repulsive for F⁻. In Fig. 2 we also show the potentials without including $V_{pol}(R)$ (dashed line), which are almost indistinguishable from the ones of Gordon and Kim [17] (empty circles, employed in Ref. [3]).

The projectile trajectory was derived from classical dynamics with the Runge-Kutta method. At every step we took into account the 256 nearest neighbor target ions (i.e. $8 \times 8 \times 4$), which includes the interaction of the projectile with the topmost atomic layer and three more layers below it. We have made sure our results do not depend on the considered number of nearest neighbors by increasing this number to include up to 8th order nearest neighbors (i.e., 8 atomic planes).

The evaluation of the eikonal transition matrix involves an integration on the starting point \vec{R}_{os} of the classical trajectory, which was calculated with the MonteCarlo technique, varying \vec{R}_{os} on the area of the unit cell as a consequence of the surface invariance. In every case we considered around 2×10^5 classical trajectories with random initial positions, and this number was varied in order to test the convergency of our calculations. The further integration on t involved in Eq. (6) was numerically solved with a relative error lower than 0.1%. To obtain the differential probability $dP/d\Omega_f$, we have to add the T-matrix elements corresponding to different values of \vec{R}_{os} that lead to the same final momentum \vec{K}_f . For this purpose we employed a grid for the angles θ_f and φ_f of 100×100 points, where θ_f and φ_f are the final polar and azimuthal angles, respectively, of the final momentum \vec{K}_f . In all calculations we oriented the \hat{x} versor along the low-index direction of the crystal surface coinciding with the impact direction; therefore, the azimuthal angle φ_f is measured with respect to the incidence direction on the surface plane (see Fig. 1). In full accord with the

experiments of Refs. [1, 2, 3] we found that under axial surface channeling conditions the relation $\theta_f^2 + \varphi_f^2 \cong \theta_i^2$ is almost strictly verified by all classically scattered projectiles and consequently, the angular projectile distribution shows the usual banana shape [18].

We start the analysis by considering the experimental case of Fig. 5 of Ref. [1]; that is, 3 keV ^3He atoms impinging on a LiF(001) surface along the crystallographic direction $\langle 110 \rangle$ with a glancing angle ($\theta_i = 1.1^\circ$). This collision system looks adequate for the eikonal description because the de Broglie wavelength of the incident atom ($\lambda = 0.0057$ a.u.) is almost three orders of magnitude smaller than the characteristic interatomic distance. In Fig. 3 we plot the differential probability $dP/d\varphi_f$, as a function of the azimuthal angle φ_f , multiplying the results by an arbitrary factor in order to show the different curves separately. The eikonal spectrum displays strong interference signatures, presenting pronounced maxima symmetrically placed with respect to the incidence direction, which corresponds to $\varphi_f = 0$. This interference pattern can be directly compared with the experimental spots of Ref. [1], which are displayed with stars, numbering them from the central one. Eikonal maxima almost perfectly agree with the experimental peaks 0, ± 1 , ± 2 and ± 3 , but the concordance deteriorates around the last peak (± 4), where an additional eikonal maximum -absent in the experiment- arises. Notice that the extreme angles of the eikonal spectrum are related to the rainbow scattering and the corresponding maxima display a sharp shape. These peaks are also present in the classical distribution, defined as the number of projectile trajectories reaching a given final azimuthal angle φ_f , which is shown in an *absolute* scale in Fig. 3. The classical scattering distribution presents the typical rainbow profile [19], with only two maxima around the extremes of the angular spectrum -the rainbow angles. Then, the absence of intermediate structures in the classical spectrum confirms the concept that interference effects are a consequence of quantum coherence between projectiles moving along different paths but ending in the same final state.

With the aim of analyzing the influence of the polarization of helium atoms, in Fig. 3 we also plot eikonal values obtained by neglecting the polarization potential; that is, by dropping the last term of Eq.(8). We found that for incidence along the direction $\langle 110 \rangle$, the angular distribution of scattered atoms is affected by the projectile polarization. When the polarization is not included in the calculation, the central maximum becomes a minimum, modifying the total number of peaks displayed by the eikonal distribution. In turn, the extreme maxima, associated with the rainbow angles, are only slightly altered by the polarization. Both angular regions - central and external- of the eikonal spectrum are associated with different zones of the interatomic potentials that are probed by axial channeled projectiles. He^0 atoms that reach azimuthal angles φ_f near 0 move over the ionic rows that form the channel, farther than 2 a.u. from

the surface, interacting with long-distance contributions of He-Li^+ and He-F^- potentials. As such contributions are dominated by the term corresponding to the polarization potential, given by Eq.(12), it explains the influence of this effect on the central zone of the spectrum. Projectiles that end in the rainbow angular region, instead, suffer close collisions with ionic centers, being affected by the short-distance behavior of the interatomic potentials, which is determined by coulombic and statistical contributions.

In Fig. 4 we investigate the elastic scattering along the direction $\langle 100 \rangle$ by considering a higher impact energy (8.6 keV). The eikonal differential probability is plotted in Fig. 4 (a) as a function of the final azimuthal angle, together with experimental spots of Fig. 2 of Ref. [3]. For this collision system, in addition to the two rainbow maxima, the eikonal distribution presents four similar peaks, symmetrically placed around $\varphi_f = 0$, and a very small central maximum. The number of main maxima of the eikonal profile coincides with that of the experimental pattern [3], although the positions of the peaks are shifted to higher values in comparison with the experimental ones. In all the cases we found that slight changes in the interatomic potentials produce substantial modifications in the angular spectrum of scattered projectiles. Hence, discrepancies between theoretical and experimental spectra could be associated with very subtle differences in the projectile-surface potential. In Fig. 4 (b) we compare experimental intensities [3] with eikonal probabilities, now plotted in linear scale, as function of the deflection angle Θ , defined as $\Theta = \arctan(\varphi_f / \theta_f)$. Taking into account that our theoretical results were obtained by considering fixed positions of the target ions, without including the thermal vibration, and they were not convoluted with experimental conditions, the eikonal model reproduces fairly well the main features of the experimental spectrum.

In order to investigate the effect of the polarization in the channel $\langle 100 \rangle$, in Fig 4 (a) we show eikonal values derived by eliminating the polarization term in Eq. (8). Remarkably, eikonal results with and without including the projectile polarization agree with each other for incidence along the $\langle 100 \rangle$ direction, indicating that polarization effects play a minor role in this channel. It is a consequence of the ordering of the halide and alkali ions involved in the axial surface channeling. As observed from Eq. (12), the polarization potentials corresponding to F^- and Li^+ have opposite signs and they compensate their contributions to order r^{-4} when F^- and Li^+ ions are placed in front of each other, as it happens in the $\langle 100 \rangle$ direction. Furthermore, within a row model, the $\langle 100 \rangle$ rows - formed by alternate cations and anions - display a neutral charge, which reduces the polarization of the incident atom. In the $\langle 110 \rangle$ direction, instead, not only are there separated cation and anion rows, with positive and negative net charges respectively, but also Li^+ and F^- ions are not in front of each other along the channel, which originates an effective polarization poten-

tial. This is the reason why polarization effects become evident for incidence along the $\langle 110 \rangle$ direction but not in the channel $\langle 100 \rangle$.

Besides, in Fig. 4 (a) we also show the angular distribution obtained within the first Born approximation [Eq.(7)], which is derived from Eq. (6) by eliminating the eikonal phase. The Born profile displays a different diffraction pattern, with a broad central maximum, not present in the experiment, indicating that interference structures of the surface eikonal model are affected by the phase η , given in Eq. (5). However, note that differences between eikonal and Born distributions vary with the considered collision system.

Finally, in Fig. 5 we considered the incidence conditions of Ref. [2], which correspond to a smaller impact energy (0.2 keV). Notice that this energy is close to the limit of validity of the eikonal model, which is expected to be adequate for high velocities. For scattering along the direction $\langle 110 \rangle$, the eikonal differential probability is displayed in Fig. 5, as a function of the azimuthal angle, comparing it with the spots of Fig. 1 of Ref. [2]. In this case, the eikonal spectrum is roughly a 55 % wider than the experimental one, corresponding to the worst disagreement found in the present work. However, both profiles - eikonal and experimental - present similar structures, with a central maximum and two additional peaks, not equally spaced, to each side. Discrepancies between the theory and the experiment can be again attributed to extremely subtle distinctions in the projectile-surface potential. Moreover, we should mention that the small displacement ($d = 0.038$ a.u.) of the surface ions with respect to their equilibrium positions introduced in our model strongly affects the interference pattern, which is almost completely suppressed when this distortion of the crystal lattice is not included. On the other hand, for incidence along the $\langle 110 \rangle$ direction (Figs. 3 and 5) we found that the angular positions of eikonal interference maxima correspond to Q_y values satisfying $Q_y = ng'$, with n an integer number, where Q_y is the component of the transferred momentum perpendicular to the scattering plane and $g' = 4\sqrt{2}\pi/a$ is the *effective* reciprocal lattice vector (a the lattice constant) that takes into account the spacing between F^- and Li^+ rows.

Again, like in Fig. 3, the central zone of the eikonal spectrum of Fig. 5 is associated with the long-distance behavior of the surface interaction, which is governed by the projectile polarization. When terms corresponding to V_{pol} are dropped, the central maximum of the eikonal distribution completely disappears, in disagreement with the experimental data.

To investigate in detail the central zone of the eikonal spectrum, in Fig 6 we plot the first ten projectile trajectories, provided by the MonteCarlo code, that contribute to the distribution at the final azimuthal angle $\varphi_f \cong 0$. For the collision system of Fig. 5 we observe that all the atoms that end in this angular region

move over F^- ions placed at the coordinate $Y = 0$. In this case, turning points corresponding to the z - movement are almost independent of the motion perpendicular to the scattering plane, being approximately situated 3.8 a.u. above the topmost atomic layer. From Fig. 6 (c), the transversal kinetic energy, defined as $E_{\perp}^{(kin)} = m_P(v_y^2 + v_z^2)/2$, slightly increases just before and after reaching the collision region, indicating that incident atoms are affected by an attractive polarization potential. The projectile-surface potential along classical trajectories, shown in Fig. 6 (d), displays an oscillatory pattern produced by the interaction with the different ionic centers of the crystal surface. Consequently, the total transversal energy $E_{\perp} = E_{\perp}^{(kin)} + V_{SP}$ presents fluctuations along the classical projectile path. However, the mean value $\langle E_{\perp} \rangle = \langle E_{\perp}^{(kin)} \rangle + \langle V_{SP} \rangle$ keeps equal to the initial value $E_{iz} = m_P v_{iz}^2/2$ along the whole trajectory, supporting the decoupling of the transversal movement from the parallel one, proposed in Ref. [2].

V. SUMMARY

In conclusion, we have developed a surface eikonal approach to deal with interference patterns produced by impact of swift atoms on insulator surfaces. The proposed method has been applied to few keV He atoms grazing impinging on LiF(001) along the $\langle 110 \rangle$ and $\langle 100 \rangle$ directions. Projectile spectra derived with the eikonal approximation display well-defined interference structures, originated by atoms that follow different paths but end scattered with the same final momentum. As the projectile distribution strongly depends on the description employed to represent the projectile-surface interaction, the study focused on the influence of the projectile polarization on the angular spectrum. We conclude that the polarization potential is essential to describe the elastic scattering along the $\langle 110 \rangle$ channel, while in the direction $\langle 100 \rangle$ its contribution is negligible. Angular spectra derived from the eikonal model, including the polarization effect, are in fair concordance with the available experimental data [1, 2, 3]. But a better representation of the surface potential, taking into account that target ions are part of a surface, might modify the present results. We think that this method may be useful to investigate very delicate items, such as long-distance potentials or crystal ion displacements, which are difficult to make evident experimentally [20].

Acknowledgments

This work was supported by CONICET, UBA, and ANPCyT of Argentina.

-
- [1] A. Schüller, S. Wethekam, and H. Winter, Phys. Rev. Lett. **98**, 016103 (2007).
 - [2] P. Rousseau, H. Khemliche, A.G. Borisov, and P. Roncin, Phys. Rev. Lett. **98**, 016104 (2007).
 - [3] A. Schüller and H. Winter, Phys. Rev. Lett. **100**, 097602 (2008).
 - [4] W.F. Avrin and R.P. Merrill, Surf. Sci. **311**, 269 (1994).
 - [5] C.J. Joachain, *Quantum Collision Theory* (North-Holland, Amsterdam, 1979).
 - [6] R.J. Glauber, *Lectures in Theoretical Physics* (Interscience, New York, 1959), Vol. 1, p. 315.
 - [7] J.R. Manson and K.-H. Rieder, Phys. Rev. B **62**, 13 142 (2000).
 - [8] A.J. García and J.E. Miraglia, Phys. Rev. A **74**, 012902 (2006).
 - [9] A. A. Abrahmson, Phys. Rev. A **133**, 990 (1964).
 - [10] M.R.C. McDowell and J.P. Coleman, *Introduction to the Theory of Ion-Atom Collisions* (North-Holland, Amsterdam, 1970).
 - [11] L. M. Hubbard and W.H. Miller, J. Chem. Phys. **78**, 1801 (1983).
 - [12] W. Lenz, Z. Phys. **77**, 713 (1932).
 - [13] H. Jensen, Z. Phys. **77**, 722 (1932).
 - [14] T. M. Miller and B. Bederson, *Advances in Atomic and Molecular Physics*, Vol. **13**, 1-55, edited by D. R. Bates and B. Bederson (Academic, New York, 1977).
 - [15] J. Vogt and H. Weiss, Surf. Sci. **501**, 203 (2002).
 - [16] E. Clementi and C. Roetti, At. Data Nucl. Data Tables **14**, 177 (1974).
 - [17] R. G. Gordon and Y. S. Kim, J. Chem Phys. **56**, 3122 (1972).
 - [18] F.W. Meyer, L. Folkerts, and S. Schippers, Nucl. Instrum. Meth. Phys. Res. B **100**, 366 (1995).
 - [19] A. Schüller, G. Adamov, S. Wethekam, K. Maass, A. Mertens, and H. Winter, Phys. Rev. A **69**, 050901(R) (2004).
 - [20] D. Farías, C. Díaz, P. Rivière, H.F. Busnengo, P. Nieto, M.F. Somers, G.J. Kroes, A. Salin, and F. Martín, Phys. Rev. Lett. **93**, 246104 (2004).

FIG. 1: Schematic depiction of the coordinate system.

FIG. 2: Scaled interatomic potentials for (a)He-Li⁺ and (b)He-F⁻. Solid lines, potential with polarization; dashed lines, potential without polarization; and empty circles, results reported by Gordon and Kim in Ref. [17].

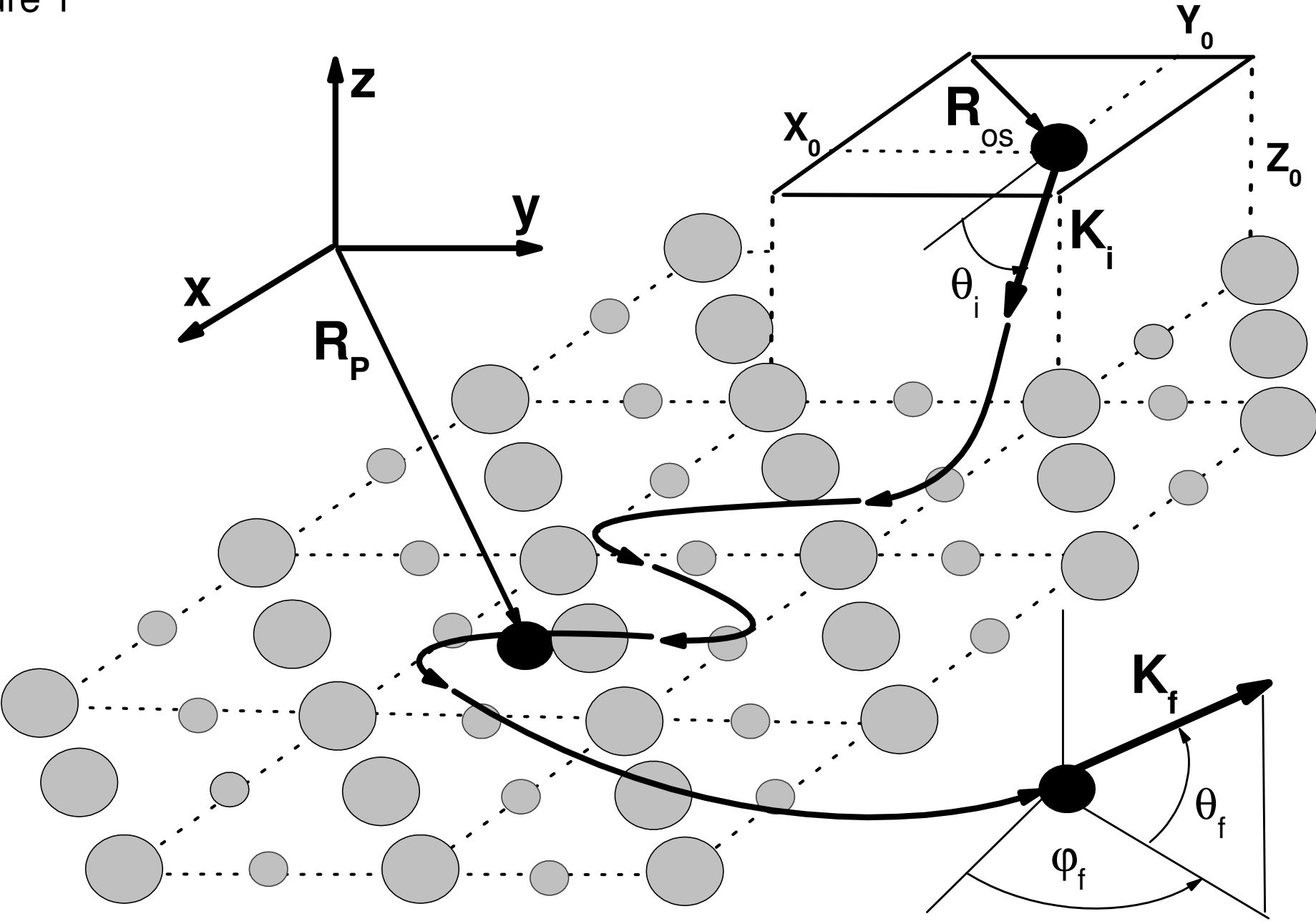
FIG. 3: Azimuthal angular distribution of elastic scattered projectiles for 3 keV ³He atoms impinging on LiF(001) along the direction <110>, with the incidence angle $\theta_i = 1.1$ deg. Solid line, differential probability derived from the surface eikonal approach, including polarization effects; dashed line, surface eikonal results without including the projectile polarization. Full stars, experimental spots of Fig. 5 of Ref. [1]. Empty circles, classical distribution, as explained in the text, in *absolute* scale.

FIG. 4: Similar to Fig. 3 for 8.6 keV ⁴He atoms impinging on LiF(001) along the direction <100>, with the incidence angle $\theta_i = 0.71$ deg. Dash-dotted line, first Born approximation [Eq. (7)]. (a) Full stars, experimental spots, and (b) thick solid line, experimental intensity, both drawn from Fig. 2 of Ref. [3].

FIG. 5: Similar to Fig. 3 for 0.2 keV ⁴He atoms impinging on LiF(001) along the direction <110>, with the incidence angle $\theta_i = 1.5$ deg. Full stars, experimental data from Fig. 1 of Ref. [2]

FIG. 6: Classical projectile trajectories ending with a final azimuthal angle φ_f near to 0, as a function of the coordinate X_P parallel to the axial channel, for the collision system of Fig. 5. (a) Coordinate Y_P perpendicular to the scattering plane; (b) coordinate Z_P perpendicular to the surface; (c) transversal kinetic energy along the trajectory, defined as $E_{\perp} = m_P(v_y^2 + v_z^2)/2$; (d) projectile-surface potential along the trajectory.

Figure 1



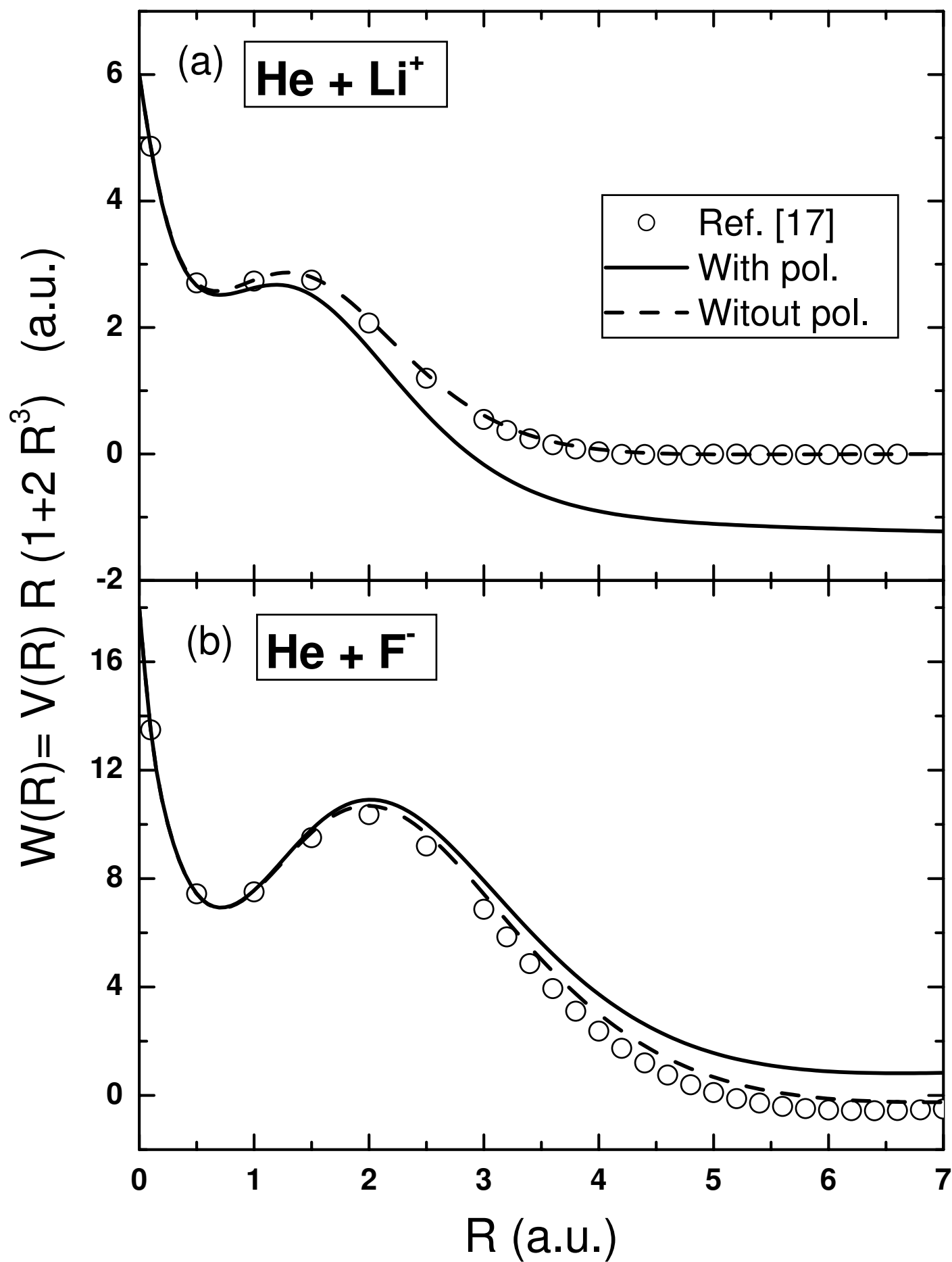


Figure 2

3 keV $^3\text{He}/\text{LiF}(001)$; $\theta_i=1.1^\circ$; $\langle 110 \rangle$

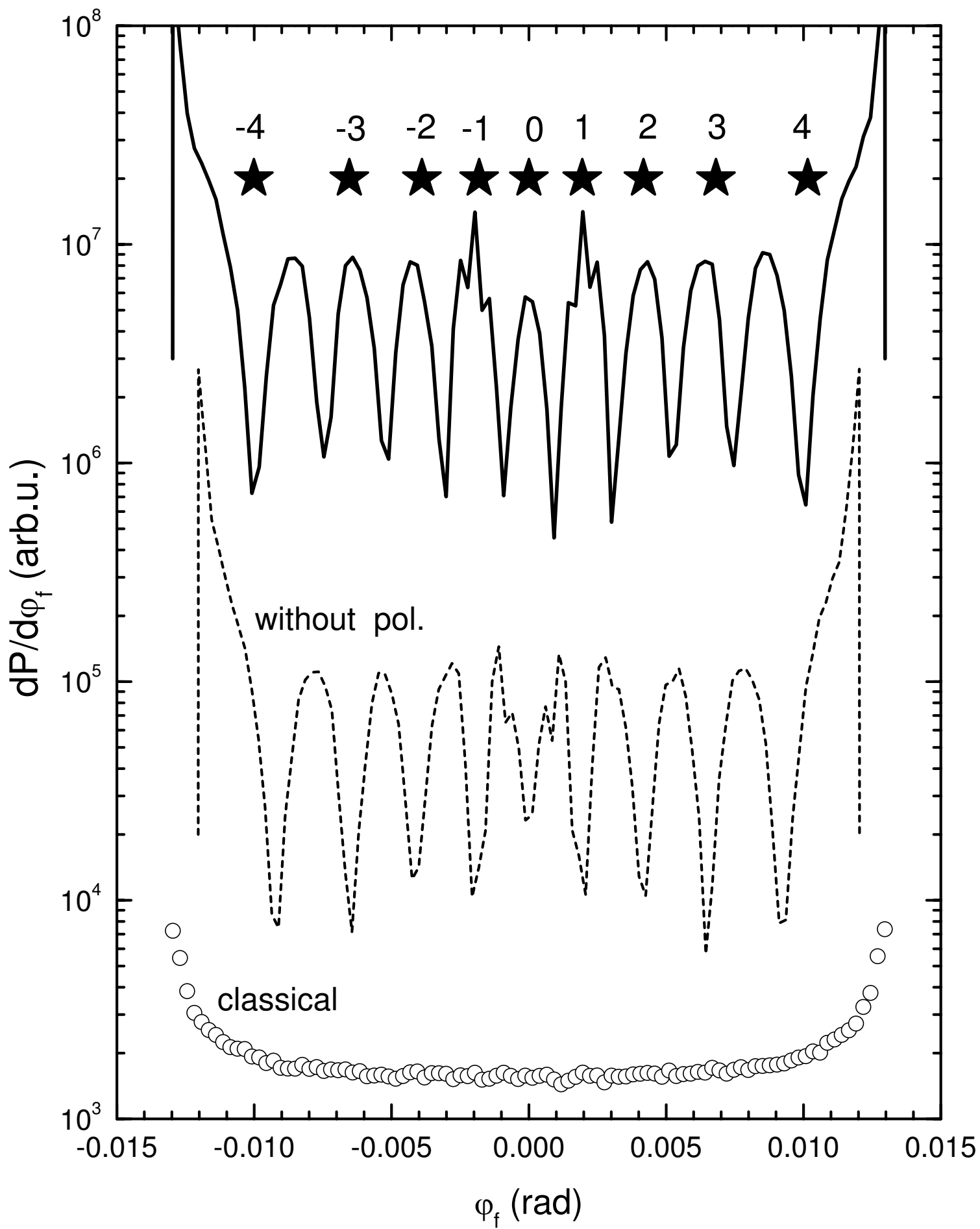


Figure 3

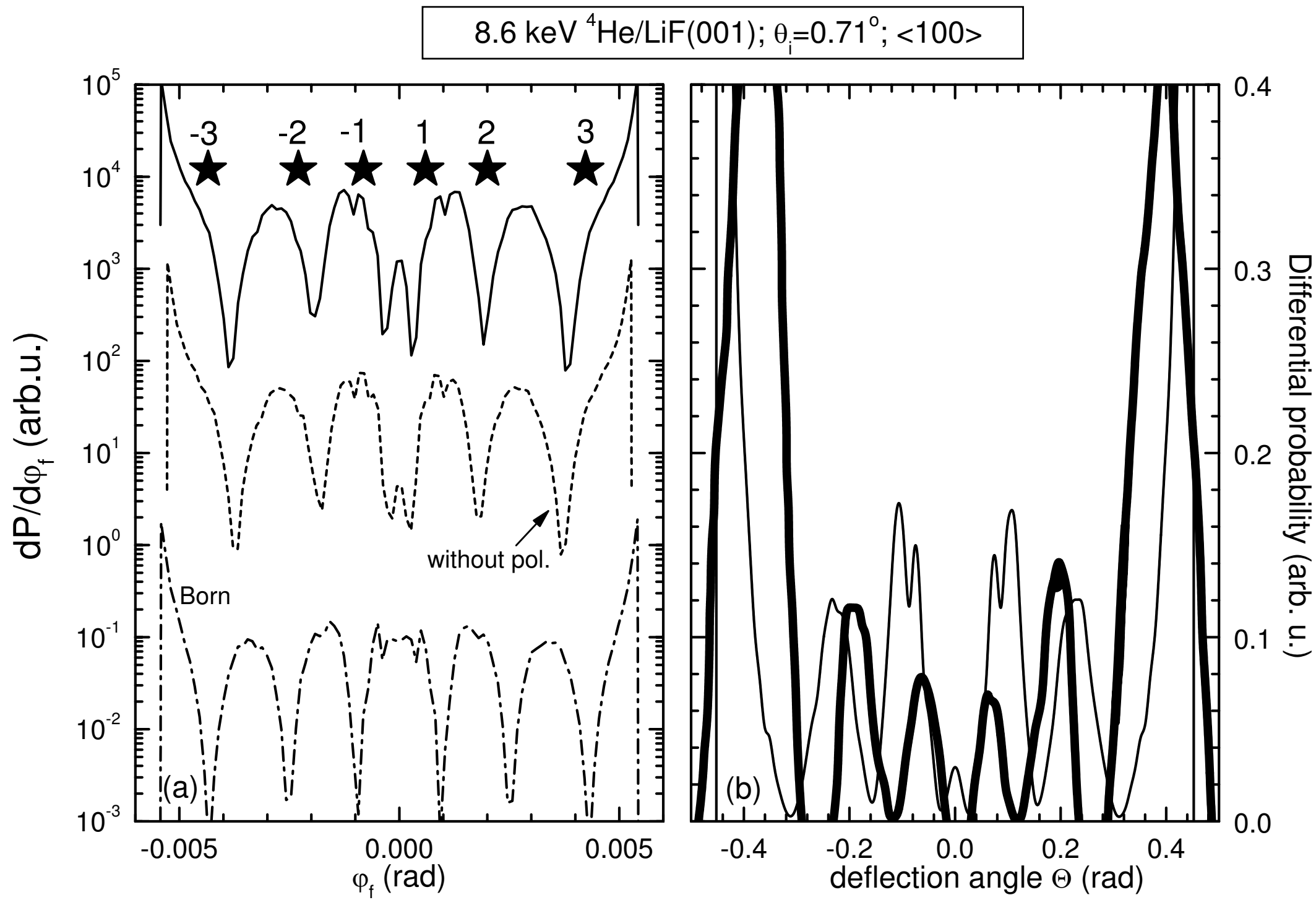


Figure 4

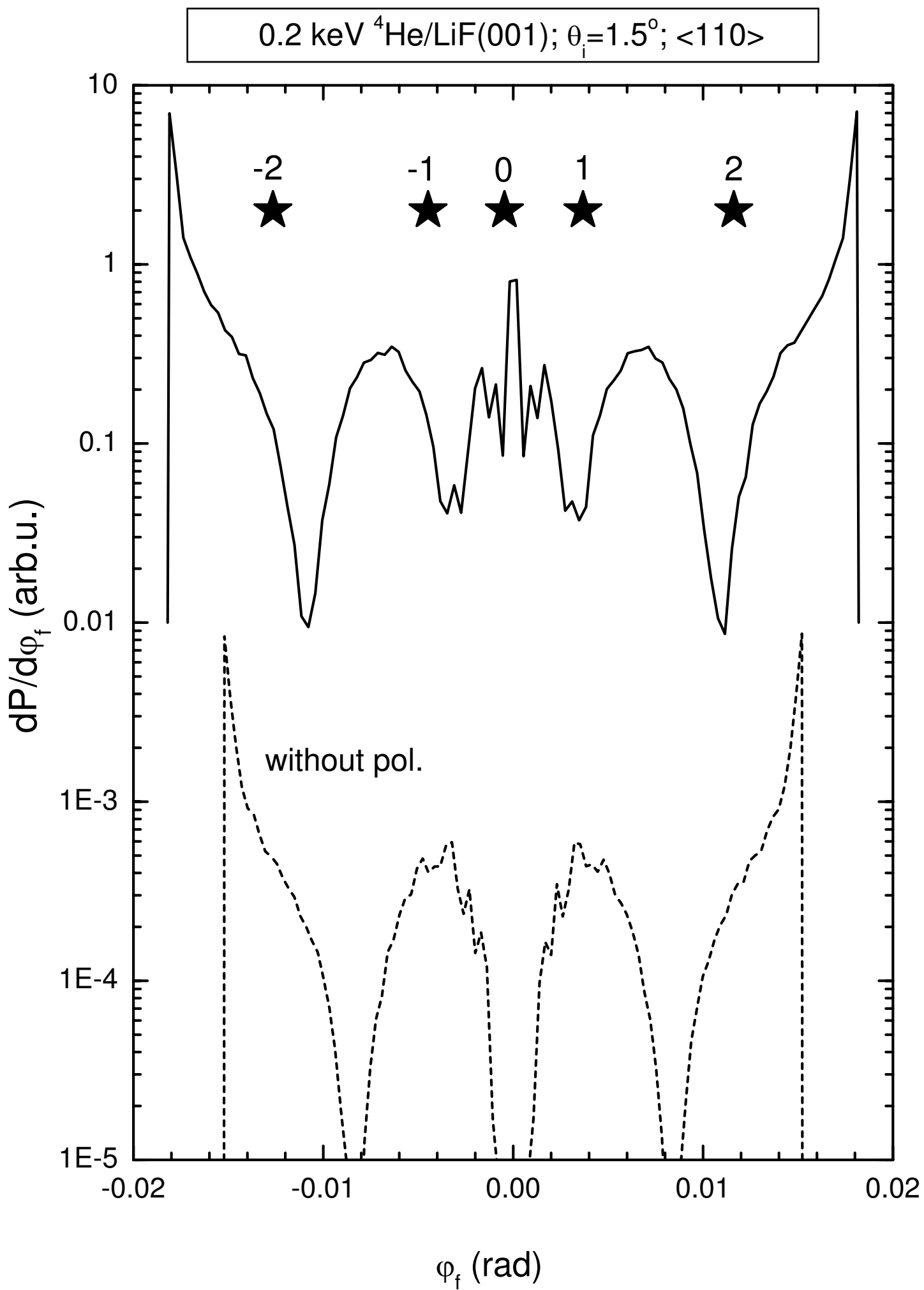


Figure 5

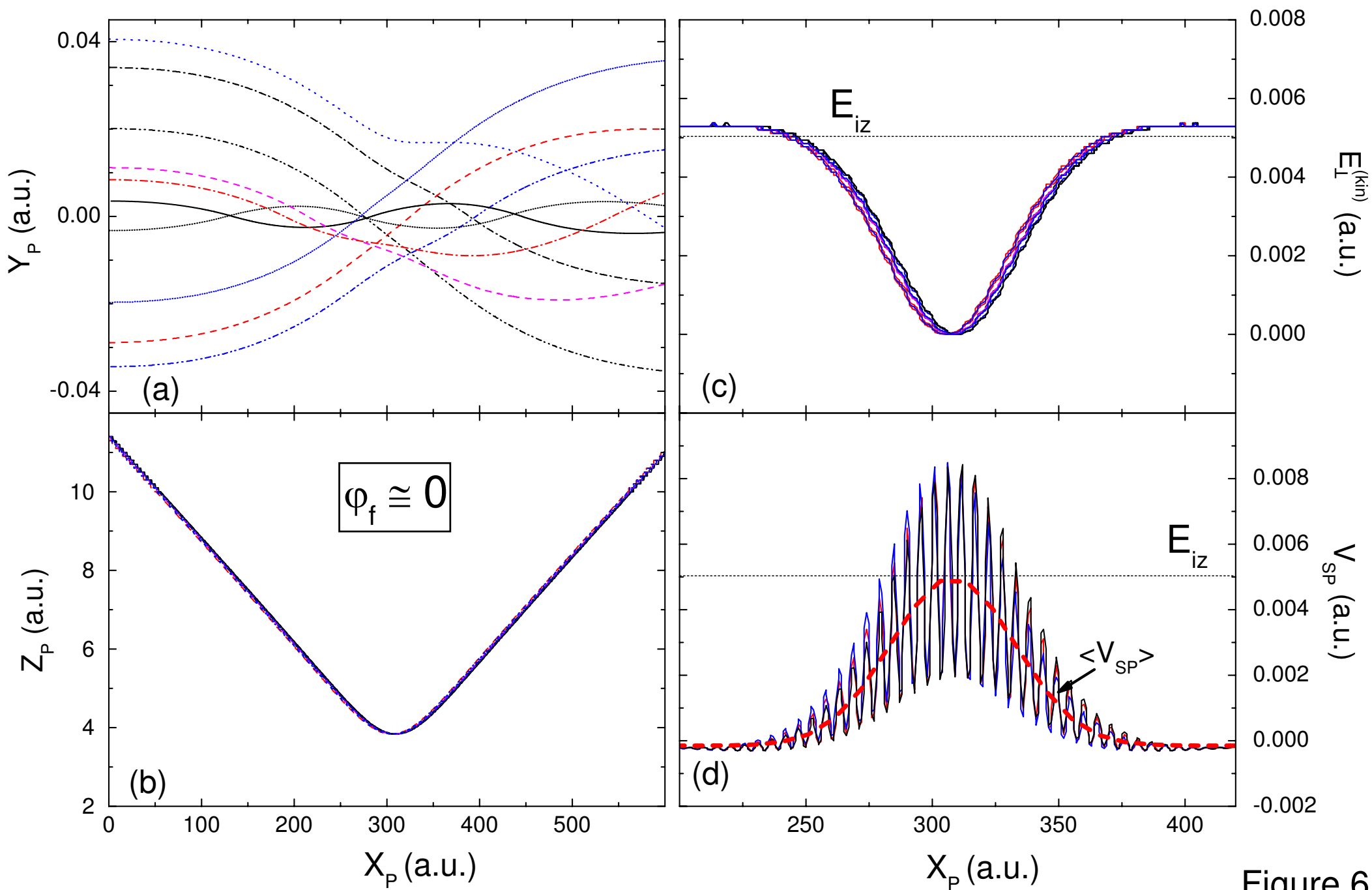


Figure 6